INORGANIC CHEMISTRY FRONTIERS

RESEARCH ARTICLE

View Article Online
View Journal

Cite this: DOI: 10.1039/d4qi00701h

How do quantum chemical descriptors shape hydrogen atom abstraction reactivity in cupric-superoxo species? A combined DFT and machine learning perspective†‡

Chandrasekhar Nettem and Gopalan Rajaraman*

Oxygen activation, a crucial function performed by enzymes, prompts the synthesis of biomimetic models utilised to investigate structure–activity relationships, with a particular focus on metal-superoxo species resulting from O_2 interaction with the metal centre. Among others, cupric-superoxo species have been extensively studied, showcasing diverse examples and potent catalytic capabilities. While quantum chemical calculations have helped in understanding the mechanistic aspect of their reactivity, recent advances in machine learning (ML) tools have substantiated this further and offered potent predictive power. The development of machine learning tools and associated quantum descriptors for open-shell paramagnetic catalysts is rarely pursued due to the complexity involved. However, if achieved, it has the potential to fundamentally change the existing paradigm in catalytic design and development. In making this connection, a detailed hydrogen atom transfer (HAT) reaction instigated by $[(\mathrm{TMPA})\mathrm{Cu}(\textsc{ii})\text{–}\mathrm{O_2}^{\bullet-}]$ species and its analogues gains relevance as they offer a unique set of diverse reactivity pathways among structurally similar cupric-superoxo species. In this study, we embark on a comprehensive exploration of reactivity mechanisms employing the DFT method (B3LYP/TZVP) with five distinct catalysts and three varied substrates, resulting in combinations that lead to fifteen different reactions for the HAT reaction. The reactivity of cupric-superoxo species was found to be correlated not only with the rate-limiting HAT barrier but also with the competitive dimerization barrier. Our comprehensive analysis of mechanisms offered a rationale for the experimentally observed reactivity and the setting of goals for developing suitable ML models. In making this connection, we have arrived at fifteen quantum chemical descriptors, including exchange interaction (J), sterics, hydrogen bonding, and various thermodynamic parameters derived from DFT calculations. Our multivariate linear regression (MLR) model accurately predicts catalytic reactivity towards HAT using these quantum chemical descriptors based simply on ground state geometry. The H-bonding interactions, along with the free energy of the HAT/PT/ET reaction ($\Delta G_{\mathrm{PCET}}/\Delta G_{\mathrm{PT}}/\Delta G_{\mathrm{ET}}$), were found to yield excellent results for accuracy (R^2 = 0.90), setting a stage to study multinuclear paramagnetic catalysts. For the first time, this study provides valuable insights not only into the reactivity of metalloenzymes but also offers design clues to enhance the reactivity of transient species using the ML approach.

Received 20th March 2024,
Accepted 11th May 2024

DOI: 10.1039/d4qi00701h

rsc.li/frontiers-inorganic

Introduction

The mechanisms of biologically essential metalloenzymes such as amine oxidases, including peptidyl glycine-α-hydroxylating monooxygenase (PHM) and dopamine-β monooxygenase (DβM), rely heavily on copper–oxygen reactive intermediates such as copper(II)-superoxo species formed from the binding and activation of dioxygen by a single copper-ion site.[1–12] Previous mechanistic studies have revealed that the substrate hydroxylation reaction mechanisms of PHM and DβM are quite similar.[13,14] Apart from these two enzymes, galactose oxidase and lytic polysaccharide monooxygenase are two other enzymes where cupric-superoxide is found to play a critical role in their functioning.[15] The copper(II)-superoxo adduct has been characterized, using X-ray structure analysis, as being present in an oxygenated precatalytic form of the PHM enzyme complex and has also been proposed in the

---

Department of Chemistry, Indian Institute of Technology Bombay, Mumbai-400076, India. E-mail: rajaraman@chem.iitb.ac.in, nettemchandrasekhar1@gmail.com

† The code and data are available through the GitHub link (**https://github.com/gopalan-rajaraman/Cusuperoxo**).

‡ Electronic supplementary information (ESI) available: Cartesian coordinates for different species and other data. See DOI: **https://doi.org/10.1039/d4qi00701h**

other enzymes based on kinetic data.[11] These enzymes perform very efficient C–H and O–H bond activation of inert substrates, and these reactions are important for the biosynthesis of prohormones and neurotransmitters in humans.[14,16–20]

While the cupric-superoxide has been found to trigger the catalytic reaction in all these enzymes, different enzymes perform different transformations – thanks to variations in their ligand environment and the protein backbone. Among other factors that contribute to their reactivity, for the end-on copper(ii)-superoxo species, its reactivity stems from the radical character of the $O_2^{\bullet-}$ moiety, which substantially reduces the barrier height for the hydrogen atom transfer (HAT) reaction, as shown in the PHM enzyme.[21] Similarly, the $\{Cu(II)–O_2^{\bullet-}\}$ species was found to be involved in the HAT of phenol in the pMMO reaction with an estimated barrier height of 35 kJ mol^{-1}. Moreover, for the LPMO enzyme as well, the HAT reaction barrier for the $\{Cu(II)–O_2^{\bullet-}\}$ species was estimated to be 21 kJ mol^{-1}.

The mechanistic studies targeting the activity of metalloenzymes are often cumbersome, and chemists have switched to smaller models that are both structural and functional mimics of metalloenzymes. Thus, there is growing interest in bioinorganic chemistry to mimic the reactivity of these enzymes *via* small structural models, and many copper(ii)-superoxo adducts are synthesized and characterized using X-ray and spectroscopic methods.[22–24] As copper(ii)-superoxo adducts are often transient in nature, spectroscopic methods coupled with theoretical tools have played an important role in their elucidation and also in understanding the implication of their electronic structure with respect to reactivity.[25–28] Over the years, more than ~50 different copper(ii)-superoxo adducts have been reported, and their reactivity patterns differ significantly from being strong to sluggish oxidants.[29,30] Although there are individual studies that have focused on the reactivity of the end-on superoxo species, due to wide variations in its coordination environment and coordination number, a general descriptor that could explain the reactivity of this species is still lacking.[29,30] Among model complexes, the oxygenation of the Cu(i) complex of the TMPA (TMPA = tris(2-pyridyl methyl) amine) ligand is one of the most extensively studied reactions, and detailed spectroscopic and reactivity studies have been reported for this species over the years.[31–35]

Most notably, Karlin and co-workers investigated the HAT reactivity of the $\{^{(X1)(X2)}LCu(II)–O_2^{\bullet-}\}$ complex (**1a**, where X1 = H, X2 = H and L = TMPA) (see Scheme 1) towards O–H bond activation using different substrates that yield $\{^{(X1)(X2)}LCu(II)–OOH\}$ species and a phenoxy radical as products.[36–38] This study was expanded later to include four more catalysts by varying substituents attached to the TMPA (X1 and X2) (**2a–5a**, see Scheme 1) that enhanced the H-bonding interactions with the $O_2^{\bullet-}$ where the reactivity was found to increase by an order of magnitude. Although H-bonding interactions were hinted at during the enhancement of the reactivity, the exact role of H-bonding interactions in the mechanism of O–H bond activation and reactivity was not studied in detail.[15] Furthermore, as a variety of substrates with structurally analogous catalysts were explored, this investigation offers a rare data set to study in detail the reaction mechanism and then employ machine learning tools[39] to develop suitable descriptors that could potentially predict the reactivity of $\{^{(X1)(X2)}LCu(II)–O_2^{\bullet-}\}$species, in general.

The bond dissociation energy (BDE),[40] H-bond (HB) interactions, frontier molecular orbital (FMO) energy,[40,41] free energy of reaction (ΔG_{PCET}),[42] steric factors,[43–45] and the asynchronicity (η)[46–48] and frustration (σ)[46] of the reaction, all of which quantify the relative capacities of different species to acquire an electron and a proton when they are vying for a hydrogen atom abstraction, were shown to play crucial roles in HAT in metal-oxo complexes. All of these parameters, however, have been shown to impact the reactivity of the metal-superoxo complexes.[26,49] Yet, there is no consensus on their individual significance or relative impact. We present a thorough statistical analysis of these parameters in copper superoxo-mediated HAT reactions. This analysis facilitates statistical exploration of various hypotheses regarding the parameters that dictate the HAT reactivity of metal-superoxo species. We developed a multivariate linear regression (MLR) model that effectively forecasts catalytic reactivity towards HAT using various quantum chemical descriptors, eliminating the need to elucidate complete mechanistic cycles, given that these are often demanding and challenging. Our findings have immediate ramifications for metal-superoxo complexes in chemical–biological systems and provide a foundation for reactivity patterns observed experimentally.

Computational methods

DFT computations employing the dispersion-corrected unrestricted Becke3LYP (B3LYP) hybrid functional[14] were used in conjunction with a double ζ quality LanL2DZ basis set with Los Alamos effective core potential for metal Cu and the 6-31G (d) basis set for the remainder of the atoms such as H, C, O, and N. This functional is chosen based on earlier benchmarking reports.[50–52] The molecular geometries were optimized without any constraints using the G09 suite of programs.[53] At the same level of theory, frequency calculations have been performed to identify the nature of the species and to compute enthalpic and entropic corrections; therefore, all the reported energies are free energies unless otherwise stated. Further intrinsic reaction coordinate (IRC) caluclations were performed on selected geometries to affirm the correct nature of the transition state, and a polarizable continuum model (PCM) was employed to incorporate solvent effects. The single-point calculations were performed on optimized geometries using the larger basis sets of TZVP for all atoms, in conjunction with the polarizable continuum model. To assess and analyse the results obtained from B3LYP functionals, we have also performed limited benchmarking studies incorporating the following functionals: PBE, BP86, PBE0, TPSSH, and ωB97X, including dispersion corrections. Using these functionals, we

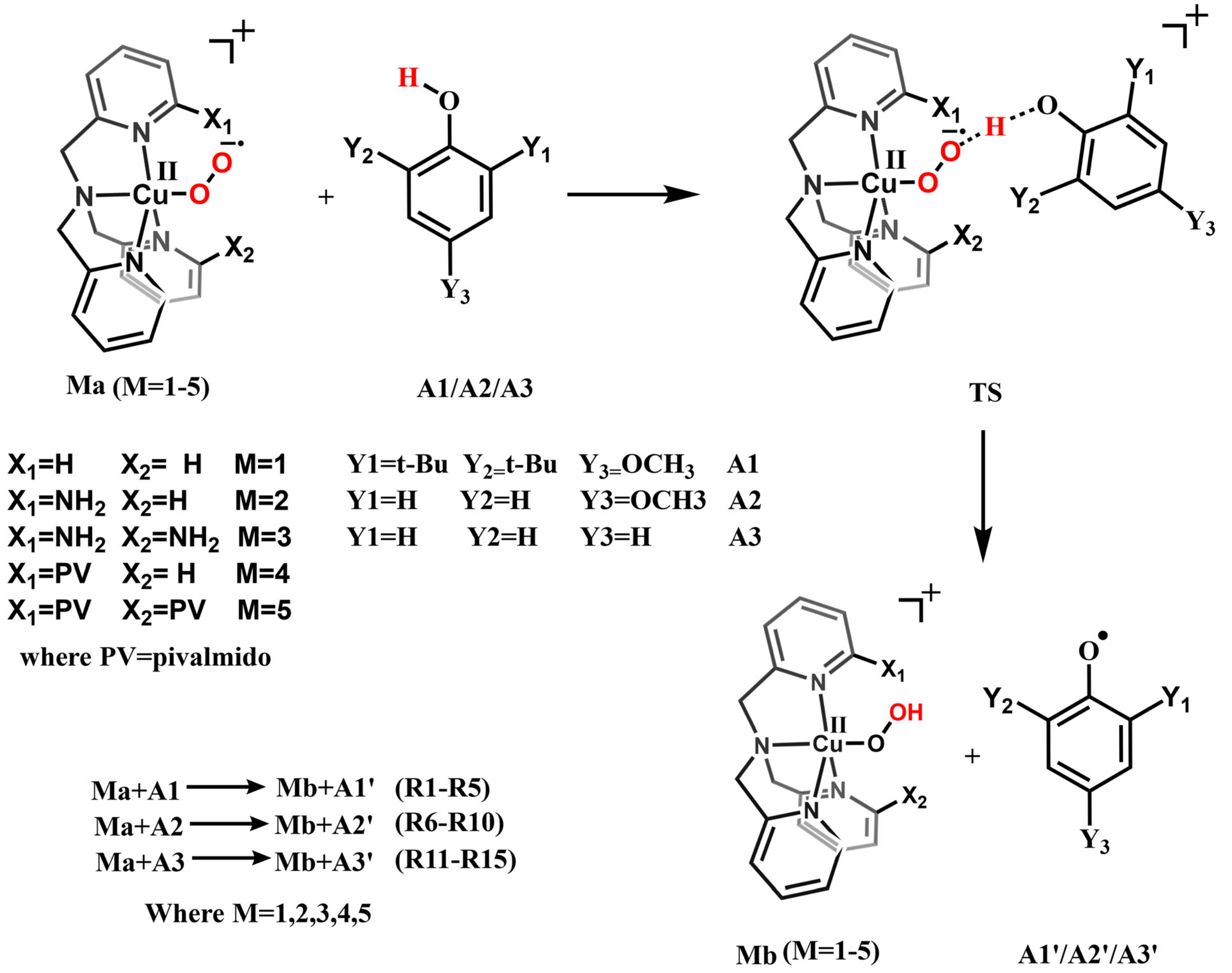

Scheme 1 Formation of {$^{(X1)(X2)}$LCu(II)–OOH} from {$^{(X1)(X2)}$LCu(II)–$O_2^{\bullet-}$} species by reacting with different phenol substrates.

have estimated the singlet–triplet gap and also the activation barrier for the HAT reaction. Tetrahydrofuran was used as the solvent employed in the experiments. Further analysis was performed on the optimized geometries, such as NBO (natural bond orbital), AIM (atoms in molecules), localized orbital locator (LOL), energy decomposition analysis (EDA), and NCI (non-covalent interactions), by employing G09 and Multiwfn 3.7.[54] The iso-surfaces of RDG were rendered by using the VMD 1.9.1 program.[55] Kinetic isotopic effect calculations were performed using the Jacob Bigeleisen equation,[56] and the tunnelling correction to the kinetic barrier was calculated using Pilgrim software employing the Page–McIver algorithm.[57,58] For all examined reactions, the minimal energy path (MEP) was followed using mass-scaled coordinates (with scaling mass = 1 amu) and Hessian computations every five steps using the Page–McIver algorithm.[58] Machine learning studies were carried out utilizing the linear regression, Lasso, Adaboost,[59] Random Forest,[60] and extreme Gradient Boosting (XGBoost) models.[61,62] The calculations of DLPNO-CCSD(T)[63,64] (cc-pvTZ; No Frozen Core and TIGHTPNO) and EPR parameters (within DFT formalism) have been performed in Orca version 4.2 software.[65] The starting coordinates for the EPR calculations have been obtained by DFT calculations in the Gaussian09 suite of programs, as stated earlier.[53] The B3LYP hybrid functional[66–68] and def2-TZVP basis set have been used for all atoms for EPR property calculations. Magnetic exchange interactions are calculated using the B3LYP functional. The magnetic exchange interaction between metal Cu(II) and the $O_2^{\bullet-}$ radical is described by the spin Hamiltonian, $\hat{H} = -J_{S1 \cdot S2}$, where J is the isotropic exchange coupling constant (see the ESI‡ for full computational details).

Results and discussion

Geometries and electronic structures of the {$^{(X1)(X2)}$LCu(II)–$O_2^{\bullet-}$} species

First, we have optimized different catalyst structures **1a–5a** (Scheme 1) used in the study. The ground-state-optimized geometries of catalysts **1a–5a** with selected structural parameters and computed spin densities are given in Fig. 1 (see ESI Tables S1 and S2 and Fig. S1 and S2‡). The unpaired electron in the

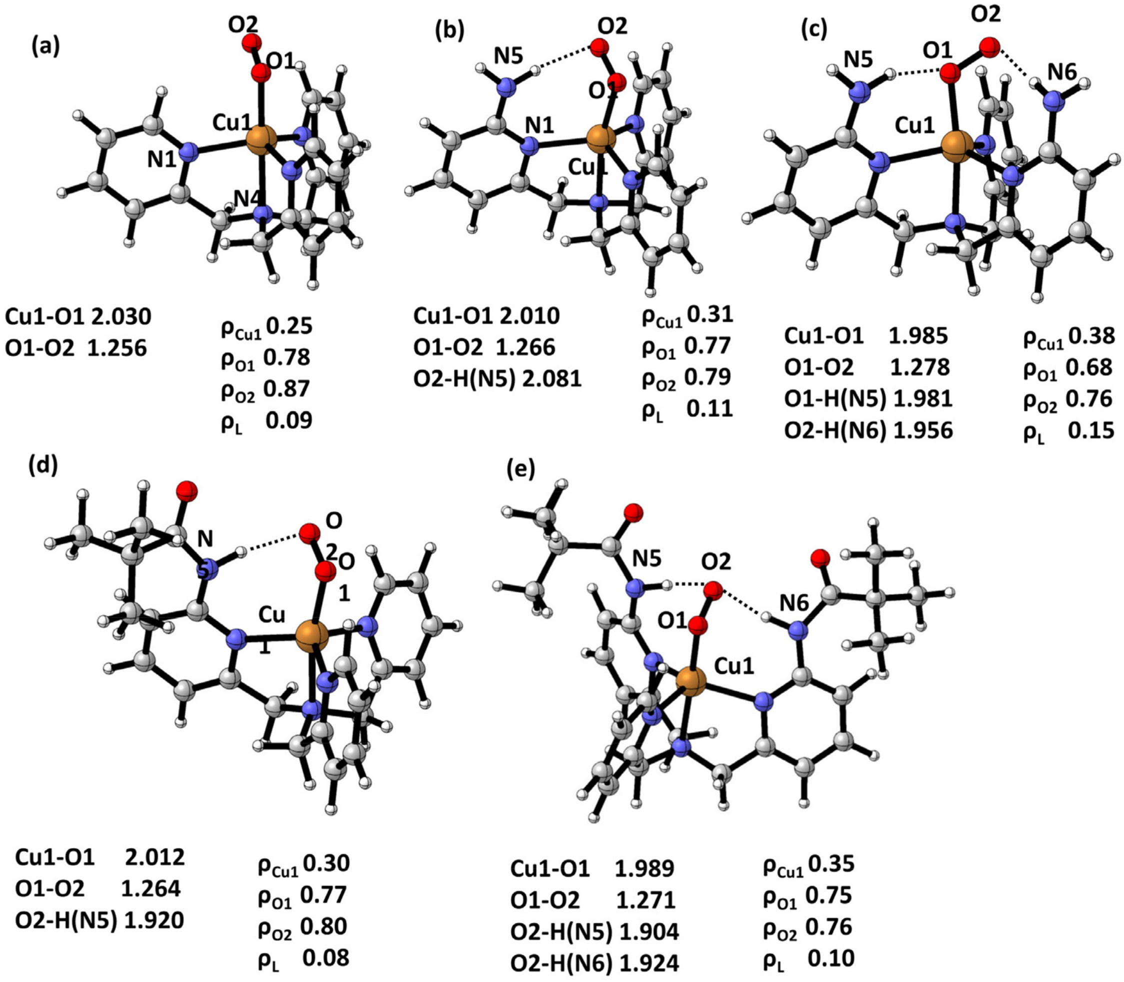

Fig. 1 DFT-optimized ground state (S = 1) geometries of catalysts **1a–5a**. (a) **1a**, (b) **2b**, (c) **3b**, (d) **4a** and (e) **5a** (all bond lengths are given in Å; ρ is spin density).

Cu(II) center and the $O_2^{\bullet-}$ are expected to have strong magnetic coupling, and therefore, we have computed both singlet and triplet states and found the triplet state to be the ground state for all complexes. The magnetic exchange interaction between $O_2^{\bullet-}$ and the Cu(II) ion is found to be ferromagnetic in nature with the exchange coupling J value estimated to be 1697.4 cm^{-1}, 1423.8 cm^{-1}, 1094.4 cm^{-1}, 1572.4 cm^{-1} and 1578.3 cm^{-1} for **1a**, **2a**, **3a**, **4a** and **5a**, respectively. With the trigonal bipyramidal geometry of the Cu(II) centre, the unpaired electron is expected to be in the d_{z^2} orbital, which would couple with the frontier orbitals of the π^*_σ with the π^*_v of the superoxo unit lying close by, and this is similar to the electronic structure established by Solomon and co-workers (see ESI Fig. S3‡).[21] A very small gap between these two π^* orbitals (π^*_σ and π^*_v) leads to a triplet ground state exemplified by the characteristic spin density shape at the superoxo unit (see ESI Fig. S1–S3‡). Similar spin density values are also witnessed for complexes **2a–5a** with slight differences in the nature of delocalization of spin density that is found to be influenced by the H-bonding interactions with the ligand framework. The spin density values on the superoxo moiety ($O_2^{\bullet-}$) and Cu(II) centre are in the range of 1.45–1.65 and 0.25–0.38, respectively. This suggests strong delocalization of spin density from the Cu(II) centre to the coordinated ligands. The singlet S = 0 state is found to be higher in energy with respect to the ground state by 100.5 kJ mol^{-1}, 96.2 kJ mol^{-1}, 100.8 kJ mol^{-1}, 93.5 kJ mol^{-1}, and 105.8 kJ mol^{-1} for **1a–5a**, respectively. The ground-state-optimized structure reveals a number of H-bonding interactions between the amino groups with proximal/distal oxygen atoms with differing strengths for complexes **2a–5a** (see ESI Table S1‡ and Fig. 1). The Cu–O and O–O bond lengths are found to be in the range of 1.985–2.03 Å and 1.25–1.28 Å, respectively, which is consistent with the expected superoxo characterisitics and experiments (see ESI Table S1‡). To understand the role of O–O rotation for different geometries, we have performed conformational analysis on catalysts by altering the dihedral angle of N1–Cu1–O1–O2 (see Fig. 1) from the *trans* to the *cis* conformation and found that the energy demand for this process is a few kJ mol^{-1} in **2a–4a** while in **5a** it is as high as 20 kJ mol^{-1} (see Table S3‡).

A closer look at the geometries reveals that complexes **3a** and **5a** possess two H-bonding interactions between the $O_2^{\bullet-}$ unit and amine H atom of the ligand (1.981 Å, 1.956 Å and 1.904 Å, 1.924 Å), and in complexes **2a** and **4a**, only one such H-bonding interaction is detected with the amide H atom of the ligand (1.920 Å and 2.081 Å; see Fig. 1 and ESI Fig. S4–S7 and Table S4‡ and related text). All these H-bonding interactions are relatively weak as the distances are longer.[69,70] To ascertain the relative strength of the H-bonding interactions and their influence on the geometry and electronic structure of these species, AIM (atoms in molecules),[71] NBO (natural bond orbital), LOL[72] (localized orbital locator) and NCI[73] (non-covalent interactions) analyses were performed.

These analyses suggest the following decreasing order of strength in H-bonding interactions: **5a** > **4a** > **3a** > **2a** > **1a** (see ESI Table S4‡ and related text). The NCI plot reveals that the catalysts **2a** and **1a** have greater van der Waals interactions (exemplified by the larger green colour points around the H bond in Fig. S4 and S5‡), while on the other hand, complexes **3a**, **4a**, and **5a** have stronger attractive intramolecular interactions (exemplified by the larger blue colour points around the H bond in Fig. S4 and S5‡). Similar to this, electron density and LOL values at the BCP (bond critical point) of the H bond in **1a**–**5a** reveal similar observations (see ESI Fig. S6 and S7 and Table S4‡). Furthermore, reactivity is impacted not only by the hydrogen-bond donating capability of substituents around $O_2^{\bullet-}$ but also by their bulkiness. Nolan and Cavallo's "per cent buried volume" (%V_{bur}) concept quantifies ligand steric effects by indicating the fraction of a ligand's volume enclosed within a sphere. To understand steric hindrance around the superoxo moiety, we calculated %V_{bur} for the catalysts in our study. Catalysts **1a**–**5a** have %V_{bur} values of 46.6, 49.8, 52.3, 51.4, and 55.1, respectively. Steric hindrance values gradually increase from **1a** to **3a**, and catalysts **3a** and **4a** exhibit similar %V_{bur} values, while **5a** demonstrates the highest steric hindrance (see Table S5‡ and related text).

Mechanism of O–H bond activation by catalysts 1a–5a

To understand the O–H bond activation by catalysts **1a** to **5a**, we have adapted the mechanism shown in Fig. 2 (see Scheme 1 and Fig. S8‡) wherein the substrate is anchored to the $\{^{(X1)(X2)}$LCu(II)–$O_2^{\bullet-}\}$ species *via* non-covalent interaction (reactant complex; **RC$_{\text{RX}}$**), followed by O–H bond activation *via* a transition state (**TS$_{\text{RX}}$**) leading to the formation of Cu(II)–OOH species and a trapped phenoxy radical (product complex **PC$_{\text{RX}}$**). In the next step, the trapped radical follows a cage-escape pathway that leads to the formation of a Cu(II)–hydroperoxo species.

DFT calculations were performed with catalysts **1a** to **5a** by considering three different substrates (*p*-methoxy-2,6-di-*tert*-butylphenol (**A1**), *p*-methoxy-phenol (**A2**) and phenol (**A3**), see Scheme 1 and Fig. S8‡), where combinations lead to a total of

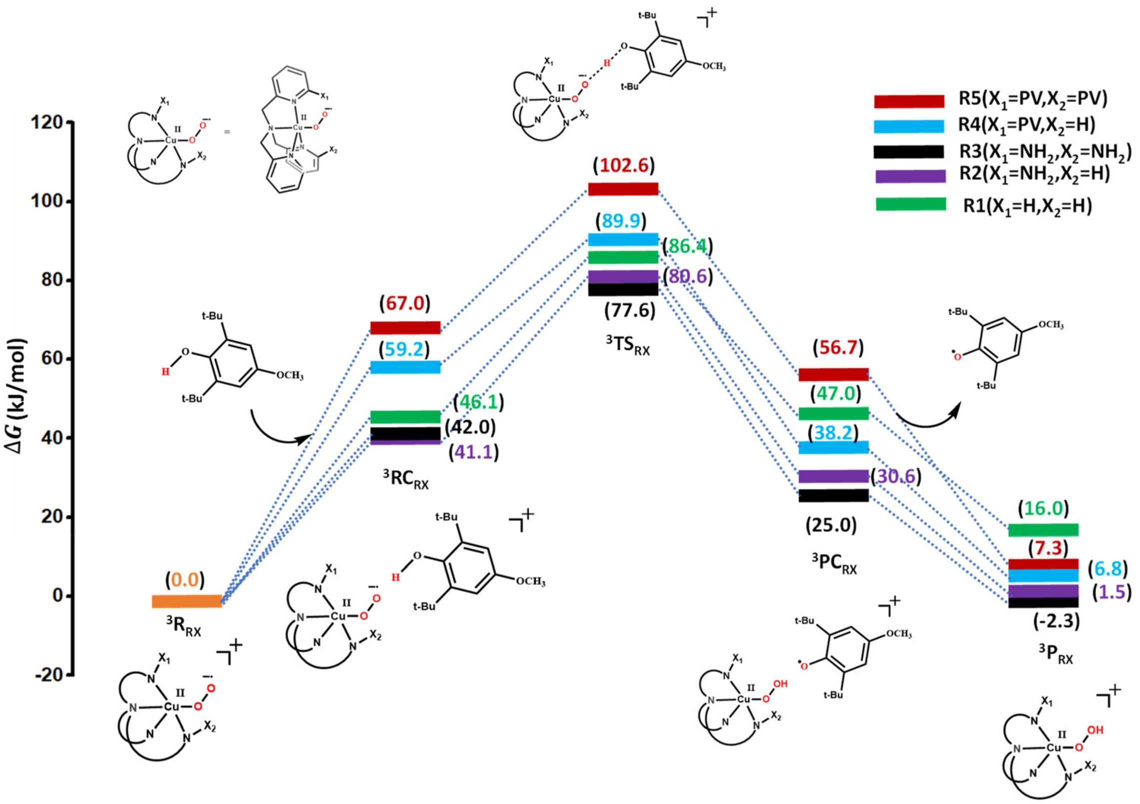

Fig. 2 Energy profile for hydrogen atom abstraction (HAT) from tertiary butyl phenol by **1a** (green; R1), **2a** (violet; R2), **3a** (black; R3), **4a** (blue; R4) and **5a** (brown; R5).

fifteen different reactions (**R1** to **R15**; see Scheme 1 and Fig. S8‡) that were modelled. For catalyst **1a** reacting with *p*-methoxy-2,6-di-*tert*-butylphenol (**A1**), the reactant complex formation (see Fig. S9 and Table S6‡) was found to be endergonic by 46.1 kJ mol^{-1}. In the next step, the O–H bond activation is assumed *via* $\mathbf{TS_{R1}}$, which is found to have a barrier height (ΔG_2) of 86.4 kJ mol^{-1} from the reactants at the triplet surface. The barrier heights computed at the singlet surface were found to be larger than 130 kJ mol^{-1}, and therefore, reactants are unlikely to participate in the reactivity. At the transition state, the newly forming O–O bond is found to be 1.280 Å with the substrate O–H bond elongating to 1.131 Å, suggesting a reactant-like transition state that is consistent with the relatively lower barrier height computed (see Fig. 3 and Table S7‡). The $^3\mathbf{TS_{R1}}$ was found to proceed *via* the σ-HAT mechanism with one β-electron from the substrate being transferred to the π^*_v orbital of the $O_2^{\bullet -}$ leading to the elongation of the O–O bond and reduction in the net spin density (see Fig. S10 and Table S8‡). A similar scenario is encountered for all the other fourteen reactions with the spin density on the $O_2^{\bullet -}$ reducing at the transition state in the range of 0.50–0.70, while the substrate gains an equivalent amount (see Table S8‡). In the next step, the $\{^{(X1)(X2)}$LCu(II)–OOH} species (**1b**) (where X1 = H and X2 = H) formed with the phenoxy radical anchored by hydrogen-bonding interactions with a significant reduction of spin density at the O–OH moiety and a concomitant increase at the Cu(II) centre (see Tables S9–S12 and Fig. S11, S12‡). The *g* value of **1b** is found to be isotropic with an estimated value of 2.08, and this matches well with the experimental data reported.[36–38] The barrier heights for catalysts **2a** and **3a** with the substrate **A1** (**R2** and **R3**) are estimated to be 80.6 kJ mol^{-1} and 77.6 kJ mol^{-1}, respectively. As the number of H-bonding interactions between substituents (amino) of the catalyst and $O_2^{\bullet -}$ is found to increase, the barrier height is found to decrease, suggesting that H-bonding interactions of the amino moiety stabilize the transition state. The barrier heights computed for **4a** and **5a** (**R4** and **R5**) with **A1** are estimated to be 89.9 kJ mol^{-1} and 102.6 kJ mol^{-1}, which are higher than that obtained for **R1**, suggesting a counter-intuitive trend based on the strength of H-bonding interactions (see Fig. 2). The computed barrier heights for **A3** (**A2**) are found to be larger (smaller) than those for **A1** (see Fig. S13 and 14‡).

Role of various factors in O–H bond activation

To understand this trend, we have performed NCI and EDA analyses, but individually, they fail to explain the trend, and this suggests a combination of factors that are at play. To gain further insights, we have examined various factors such as (i) the free energy of reaction (ΔG_{PCET}), (ii) the strength of H-bonding (HB) interactions, and (iii) buried volume (BV) on reaction barriers *via* least squares regression. These analyses suggest that ΔG_{PCET} accounts for only 20% of the dataset variation. However, if the BV is added, this substantially improves the R^2 value to 0.81. The inclusion of HB does not yield any significant improvement (see Fig. S15‡). As BV is estimated to be an important parameter, the reason for such a close correlation was explored by computing the strain energy associated with the substrate (NCI plots support these observations) (see Fig. S16 and 17‡). This provided a significant correlation on its own (see Fig. S17 and Table S13‡), and suggests that the prevailing influence of steric hindrance over H-bonding interactions emphasizes the critical importance of H-bond donor groups being relatively compact yet possessing a higher H-bonding capacity to effectively lower the reaction barrier for HAT.

Understanding the impact of quantum tunneling in the hydrogen atom transfer (HAT) reaction

Apart from the kinetic barrier, a meticulous examination of the imaginary frequencies associated with the corresponding transition states (refer to Fig. 3) indicates the potential involvement of tunnelling. This aspect, as demonstrated by Shaik and co-workers, has been elucidated as crucial in comprehending the reactivity of metal-oxo species.[74–79] To understand the role of tunnelling, we have computed the Wigner transmission coefficient values[79] for catalysts **1a**–**5a** with substrate **A1** (**R1**, **R2**, **R3**, **R4**, and **R5**). These are estimated to be 3.24, 2.81, 1.99, 2.21, and 1.23 for **R1**–**R5**, respectively. As the strength of H-bonding interactions and extent of bulkiness were found to increase (**1a**–**5a**), the transmission coefficient was found to decrease, suggesting that H-bonding interactions and bulkiness of substituents play crucial roles in dictating the tunnelling. Overall, both the H-bonding interactions between substituents (amino/pivalamido) of the catalysts and the $O_2^{\bullet -}$ radical, and the steric hindrance between substituents (amino/pivalamido) of the catalysts and the substrate were found to decrease the transmission coefficient (see Tables S14–S16‡). Furthermore, we have also estimated the kinetic isotopic effect (KIE) values at 298 K, which were found to be 6.0, 5.7, 4.8, 5.2 and 5.6 for **R1**–**R5**, respectively (see Fig. S18 and related text, and Tables S17–S20‡). The KIE values also predict a similar trend to that of the tunneling coefficient calculations affirming confidence in the methodology employed.

Role of thermodynamic stability of the catalysts

Not only do the kinetics, thermodynamics, and tunnelling of the HAT reaction affect its overall rate but they also affect the rate of competitive reactions such as (i) the formation of the Cu(I) precursor complex from the $\{^{(X1)(X2)}$LCu(II)–$O_2^{\bullet -}\}$ complex by releasing oxygen and (ii) the formation of 2 : 1 Cu/O_2 or *trans*-μ-1,2-peroxide species ($\{^{(X1)(X2)}$LCu(II)–O–O–Cu(II)$L^{(X1)(X2)}\}$) from the $\{^{(X1)(X2)}$LCu(II)–$O_2^{\bullet -}\}$ complex by reacting with the Cu(I) precursor complex (see Scheme 2). The free energy of reaction (ΔG_1°) for the formation of $\{^{(X1)(X2)}$LCu(I)} precursors (^{1}**1c**–^{1}**5c**) from their respective $\{^{(X1)(X2)}$LCu(II)–$O_2^{\bullet -}\}$ complexes (^{3}**1a**–^{3}**5a**) is around −5.1 kJ mol^{-1}, −12.9 kJ mol^{-1}, −13.0 kJ mol^{-1}, −20.8 and −23.4 kJ mol^{-1} for **1a**–**5a**, respectively (see Fig. 4 and Tables S21–S25‡). The relaxed scan performed by varying the Cu1···O1 distance shows that the formation of Cu(I) precursors (^{1}**1c**–^{1}**5c**) from their respective $\{^{(X1)(X2)}$LCu(II)–$O_2^{\bullet -}\}$ complexes (^{3}**1b**–^{3}**5b**) is a barrierless process for all of the catalysts, with the exception of ^{3}**5a** (see Fig. S19‡).

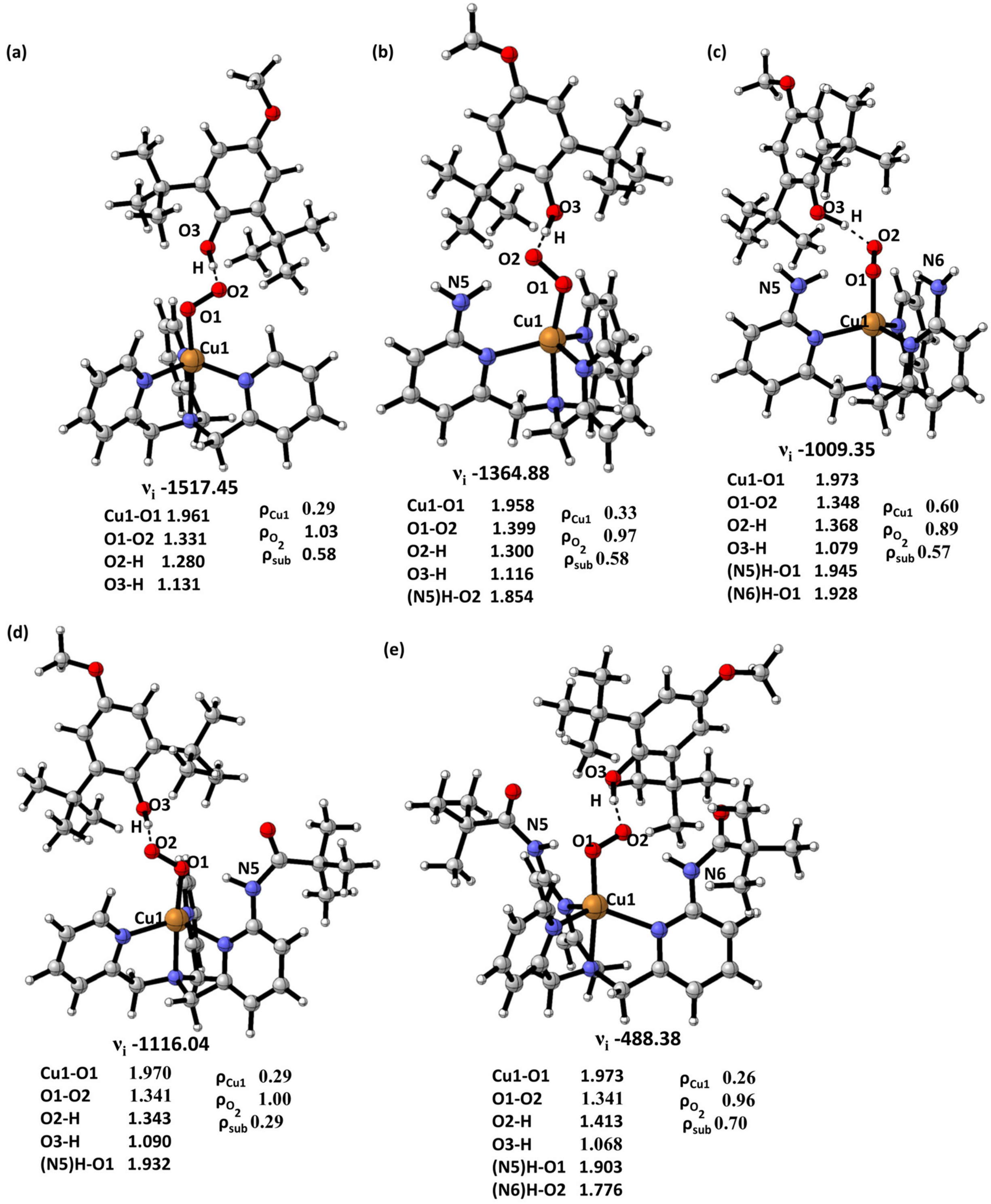

Fig. 3 DFT-optimized geometries of the transition state (*S* = 1 spin state): (a) $^3\mathbf{TS}_{\mathbf{R1}}$, (b) $^3\mathbf{TS}_{\mathbf{R2}}$, (c) $^3\mathbf{TS}_{\mathbf{R3}}$, (d) $^3\mathbf{TS}_{\mathbf{R4}}$ and (e) $^3\mathbf{TS}_{\mathbf{R5}}$ (all bond lengths are given in Å and frequencies are in given cm^{-1}; ρ is spin density).

Furthermore, ΔG_1° is found to decrease with increasing hydrogen-bond donor ability and steric hindrance of the substituent attached to the TMPA ligand. The activation free energy of the reaction (ΔG_3) for the formation of 2 : 1 Cu/O$_2$ or *trans*-μ-1,2-peroxide species (^{3}**1d**–^{3}**5d**) from their $\{^{(X1)(X2)}\mathrm{LCu(II)–O_2}^{\bullet-}\}$ complexes (^{3}**1a**–^{3}**5a**) by reacting with $\{^{(X1)(X2)}\mathrm{LCu(I)}\}$ precursor (^{1}**1c**–^{1}**5c**) complexes is estimated to be 55.8 kJ mol^{-1}, 60.6 kJ mol^{-1}, 71.4 kJ mol^{-1}, 82.0 kJ mol^{-1} and 96.9 kJ mol^{-1} for **1a**–

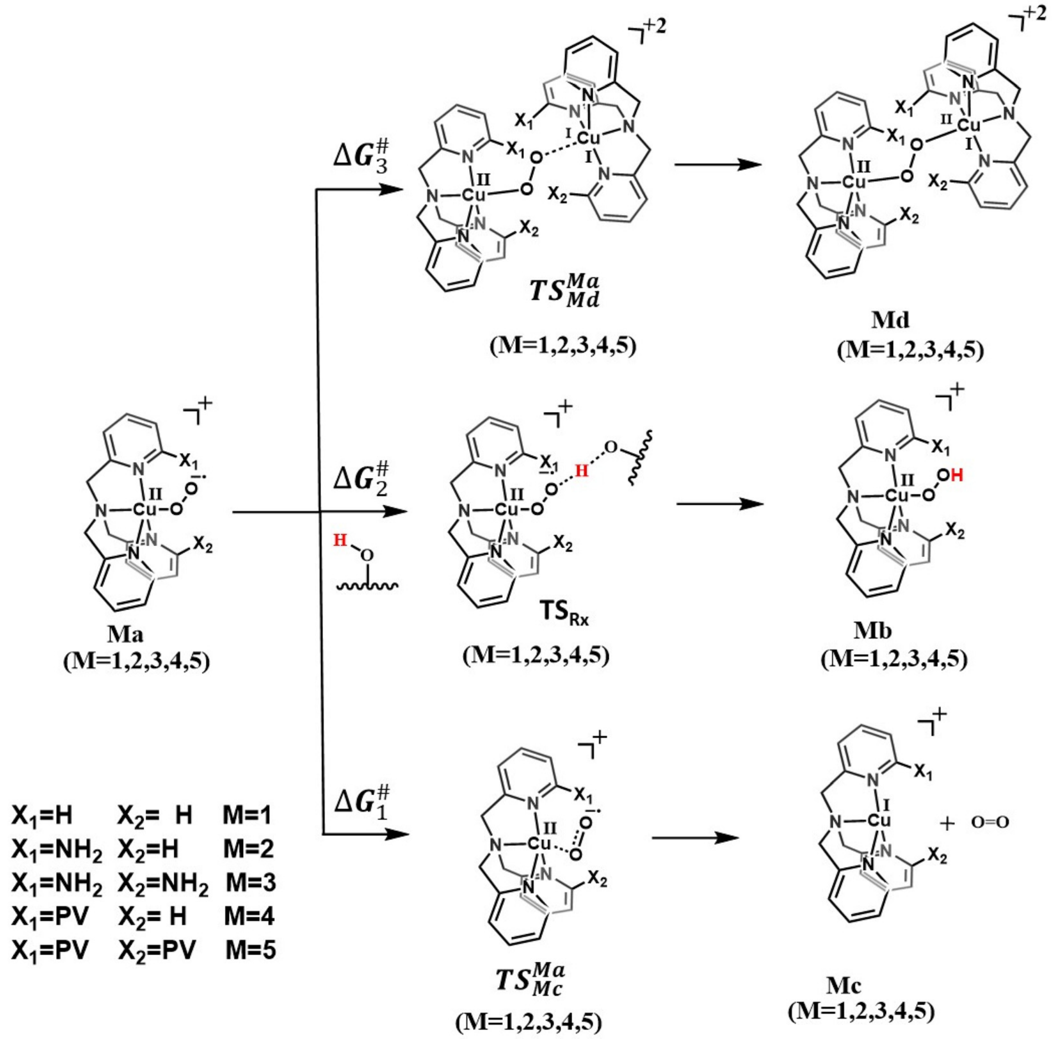

Scheme 2 Adapted mechanism of reactivity and the decomposition pathways of the {$^{(X1)(X2)}$LCu(II)–O$_2^{\bullet-}$} species.

5a, respectively, following the order **5a** > **4a** > **3a** > **2a** > **1a** (see Fig. 4, Fig. S20‡ for transition state geometries and Tables S21–S25‡ for transition state structural parameters and spin densities).

This trend is in agreement with the experimental trend of decomposition rate constants estimated from absorption spectra.[80] The S = 0 (both open-shell and closed-shell singlets) spin state of species **1d**–**5d** is found to be more than 60 kJ mol^{-1} higher in energy compared to the S = 1 state (see Table S23‡). In ^{3}**1d**, the Cu⋯Cu separation is found to be 4.532 Å, which also matches with that of the reported X-ray structure[10,81] (see Fig. S21 and Tables S21–S25‡). To obtain quantitative insights, we examined the role of HB and BV on the activation free energy of reaction (ΔG_3) for the formation of 2 : 1 Cu/O$_2$ *via* least squares regression. Both BV and HB alone were found to correlate well, yielding a value of more than 0.83R^2 (see Fig. S22‡), while the combination of both BV and HB does not result in significant improvement. The overall catalytic reactivity was found to be correlated with the difference between ΔG_2 and ΔG_3 termed as ΔG_{total} ($\Delta G_{\text{total}} = \Delta G_2 - \Delta G_3$) and follows the order **1a** < **2a** < **3a** ∼ **4a** < **5a** for substrate **A1**, which is aligned with the experiments (see Table S26‡).[8,80]

Comparative analysis of reactivity: machine learning *versus* valence bond predictive models

In recent years, the study of catalytic mechanisms and the creation of new materials have both benefited greatly from the use of machine learning (ML) models.[82,83] These may be used in conjunction with DFT computations to determine the underlying connection between the theoretical indications and descriptors.[84] Other than the ML models, there are also other approaches, such as the valence bond (VB) model, that have been shown to successfully predict the reactivity pattern in metal-oxo species.[42,85] The proposed equation for estimating the activation barrier is based on DFT-computed (or experimental) bond dissociation energies of reactants and products

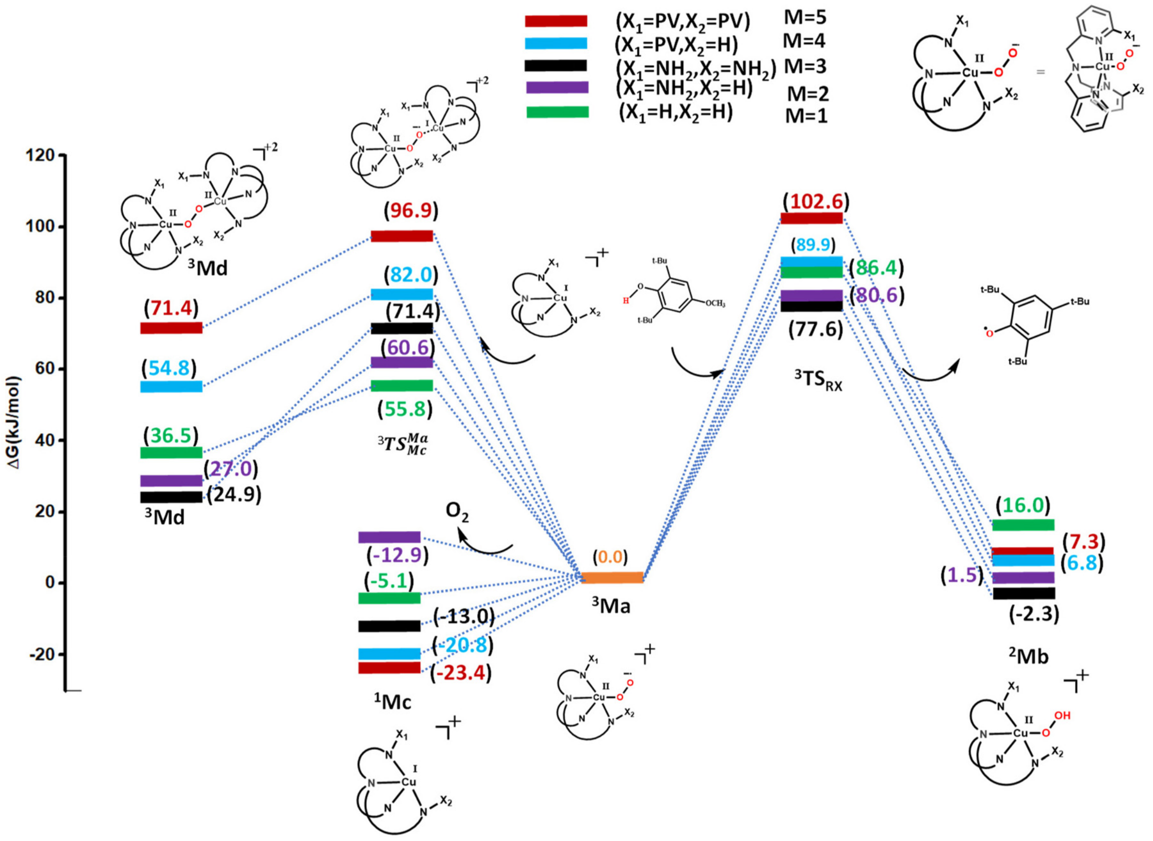

Fig. 4 DFT-computed potential energy surface for the formation of binuclear Cu species from the Cu(II)-superoxo species.

and is adapted from the work of Shaik and co-workers[42] (eqn (1); see Fig. S23‡ and related text for details):

$$\Delta E^{\#}_{\mathrm{VB}}(2) = 0.3G_0 + 0.5\Delta E_{\mathrm{rp}} - B_{\mathrm{XHY}} + 0.5\left(\frac{\Delta E_{\mathrm{rp}}{}^2}{G_0}\right) \quad (1)$$

where,

$$B_{\mathrm{XHY}} = \frac{1}{4}[\mathrm{BDE}_{\mathrm{H-X}} + \mathrm{BDE}_{\mathrm{H-Y}}] \quad (2)$$

and

$$G_0 = 0.5(G_{\mathrm{r}} + G_{\mathrm{p}}) \quad (3)$$

$\mathrm{BDE}_{\mathrm{H-X}}$ is the BDE of $\{^{(X1)(X2)}\mathrm{LCu(II)–OOH}\}$ and $\mathrm{BDE}_{\mathrm{H-Y}}$ is the BDE of the substrate. Here, ΔE_{rp} is the energy difference between the reactant and the product. The G_{r} and G_{p} terms are promotion gaps (see Fig. S23‡). Using this equation, we have estimated the barrier height for **R1–R15** (see Table S27‡) and the regression model, based on the ΔE_{VB} *vs.* the computed barrier height (ΔG_2), which was found to yield a poorer prediction of the barriers (the R^2 value is 0.25; see Fig. S24‡). The complexity observed in understanding the reactivity of metal-superoxo species can be ascribed to the presence of radical species at both the catalyst and substrate (radical), leading to intricate spin patterns. Additionally, the steric properties of the ligands and the approach of the substrate are pivotal factors influencing the reaction. To illustrate this point, we have considered a scenario where both ΔE_{VB} and BV are taken together into consideration, and this model is found to yield an improved correlation (R^2 = 0.80; see Fig. S24‡).

Machine learning models

It is clear from the earlier analysis that a combination of factors (not only BDE) is needed to rationalize the experimental reactivity and also for prediction. Keeping this in mind, we have moved to machine learning models with our data set of **R1–R15** and have developed various descriptors using multivariable linear regression (MLR) models to predict the target variable. This approach leveraged all available data, revealing factors influencing the reactivity.

We have considered a total of fifteen descriptors (termed as features *i.e.*, F01–F15) spanned over five categories such as (i) steric and hydrogen bonding (F01, F13), (ii) frontier orbital energy and magnetic coupling (F14) (see Computational methods), (iii) thermodynamic quantities (F05, F06, F07, F08, F09, F15) (see Fig. S25‡), (iv) bond-dissociation energy (F02, F03), and (v) acido-basic and redox potential quantities (F10, F11, F12) (see Fig. 5(a) see Fig. S26‡). Importantly, none of these parameters requires transition state geometries (see Tables S28 and 29‡), or the estimation of kinetic barriers, which is not only a challenging task but, given the open-shell nature of the reaction, often involves multiple spin states and

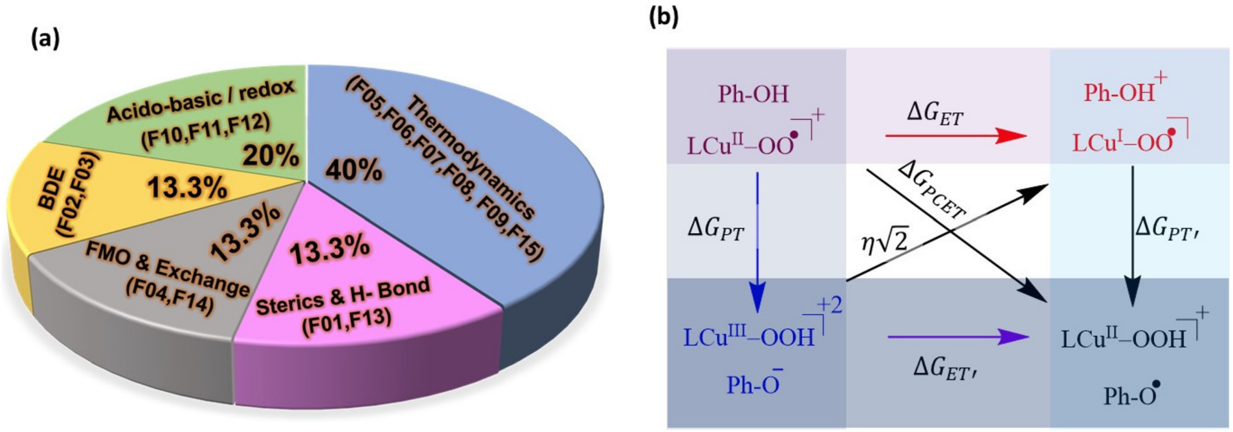

Fig. 5 (a) The descriptors used in the ML model employed. (b) Schematic representation of various thermodynamic descriptors employed.

spin coupling that may lead to the possibility of even missing the lowest energy transition state.[86,87] Furthermore, a robust ML model based on simple quantities adapted here can help to pave the way forward for larger screening and more robust prediction.

To assess the mutual relationship or correlation among the selected descriptors, we computed the pair-wise correlation coefficient between them (see Fig. 6). The pair-wise correlations between different descriptors and target variables T01 (ΔG_{total}) and T02 (ΔG_2) are assessed using the Pearson correlation coefficient, and the findings are shown in Fig. 6. Highly positive or highly negative correlation coefficients, which suggest significant correlation between the pair of descriptors, are indicated by dark red or blue colours. The BDE energy-based descriptors were found to be not correlated at all to the T01 parameter, while with T02, the correlation is weak. Given the fact that the BDE of the substrates is widely used by experimentalists to correlate with the reactivity, our work suggests a note of caution in this approach, especially when competing reactions are operational. Among the descriptors, the magnetic coupling J between the Cu(II) centre and superoxo $O_2^{\bullet-}$ radical is also considered, given the fact that this can be estimated using experiments and can also be calculated using DFT methodology with good numerical accuracy.[88] Furthermore, earlier work implicates the role of magnetic coupling in the C–H bond activation barriers for the metal-superoxo species.[89] In the given data set, while J is found to have a reasonably good correlation to the target variable T02, for the overall energetics that dictate the reactivity, which includes the dimerization reaction, *etc.*, the correlation is found to be rather weak.

Furthermore, the high values of the Pearson correlation coefficient suggest that some of the descriptors, such as F07 (ΔG_{ET}), F13 (HB) and F15 ($\sigma = \Delta G_{\text{PT}} + \Delta G_{\text{ET}}$) are significantly correlated with the target variable T01. The training set and the testing sets for ML models are made up of 15 sets of data, which are randomly divided into 12 sets and three sets. Through an iterative multivariate regression modelling process, the four-component model was identified to predict T01, which is given by eqn (4) (see Fig. 7 and Tables S30, S31‡) (for the T02 variable, see Fig. S27 and Tables S32–S33‡):

$$\begin{aligned}\Delta G^{\#}_{\text{tot}} &= 8.3484(\text{HB}) - 18.7055(\Delta G_{\text{PCET}}) \\ &\quad - 4.5758(\Delta G_{\text{PT}}) + 21.8389(\Delta G_{\text{ET}}) + 13.7749\end{aligned} \tag{4}$$

For the T01 variable, the model is able to predict the target variable with an R^2 of 0.90 (test set), RMSE of 4.01, and an MAE of 3.2 kJ mol^{-1} (for the test set), yielding excellent accuracy for this complex reaction. The regression model's performance was tested using four-fold cross-validation (MAE = 4.36 kJ mol^{-1}) and LOO (leave one out) (MAE = 3.38 kJ mol^{-1}). To validate the model developed, we have extended our studies to two new Cu(II)-superoxo species reported earlier by Karlin and co-workers[90] (see Fig. S28 and Tables S38, S39‡), which were experimentally tested to exhibit HAT reactions. We then employed the aforementioned ML model to compute the barrier height for these two catalysts. Our ML model displayed strong generalization for these two unseen hydrogen atom transfer reactions with a mean absolute error of 6.4 kJ mol^{-1} against DFT-computed barriers, further validating the predictive capability beyond the tested sample space.

The observed dependence on ΔG_{PT} and ΔG_{ET}, as revealed by our linear regressions, aligns with theoretical models documented in the literature.[41] The dependence of catalytic activity on ΔG_{PCET} is well documented in the literature (Bell–Evans–Polanyi principle)[91,92] and the reliance on ΔG_{PT} and ΔG_{ET} likely stems from the amalgamation of proton transfer and electron transfer intermediates into the concerted transition state.[41] In the broader dataset, we note that ΔG_{ET} and ΔG_{PCET} exert a more pronounced influence on the total of the reaction barriers compared to either ΔG_{PT} or HB (H-bond strength). This is evident in the larger coefficient assigned to the ΔG_{ET} and ΔG_{PCET} terms relative to the coefficients for the ΔG_{PT} and HB (H-bond strength) terms in the fitting equation (see Tables S30 and S31‡). While the role of thermodynamic quantities influencing the reaction rate is evident in the literature,[41] H-bonding interaction was found to have more influence than the ΔG_{PT} parameter, emphasizing the importance of weak

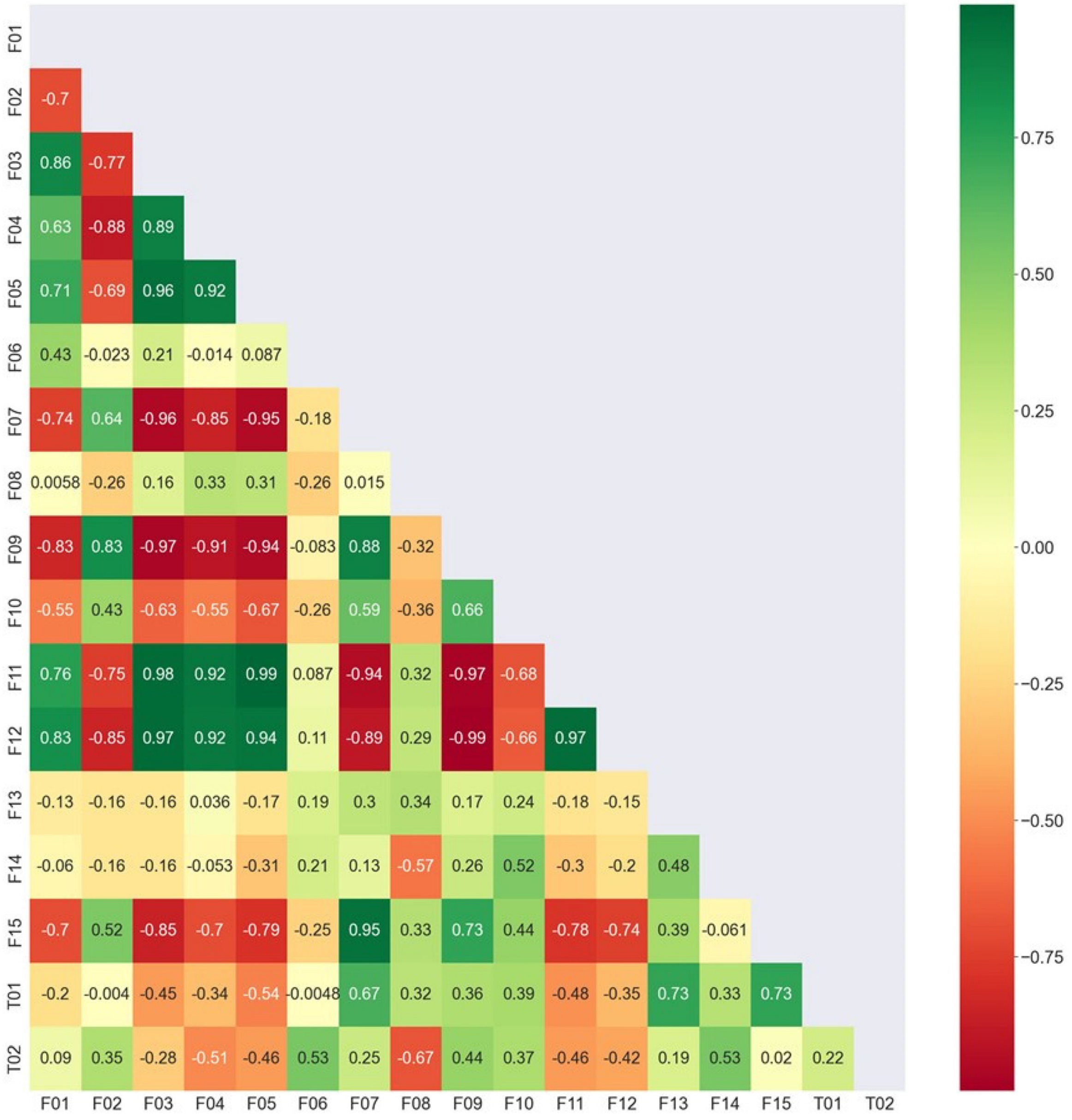

Fig. 6 Heat map illustrating the pairwise relationship between quantum chemical descriptors and target variables (ΔG_2 and ΔG_{total}) [F01 – BV_{tot}, F02 – $\sum E_{\text{BDE}}$ (kJ mol^{-1}), F03 – ΔE_{BDE} (kJ mol^{-1}), F04 – E_{FMO} (eV), F05 – η (meV), F06 – λ (meV), F07 – ΔG_{ET} (kJ mol^{-1}), F08 – ΔG_{PT} (kJ mol^{-1}), F09 – ΔG_{PCET} (kJ mol^{-1}), F10 – $\Delta P^{k_a}_{\text{eff}}$, F11 – $\Delta E^{\circ}_{\text{eff}}$ (meV), F12 – $\Delta E°(H)$ (meV), F13 – HB (kJ mol^{-1}), F14 – J (cm^{-1}), F15 – σ (kJ mol^{-1}), T01 – ΔG_{tot} (kJ mol^{-1}), T02 – ΔG_2 (kJ mol^{-1})].

non-covalent interactions in modulating the reactivity. Given the fact that the metal-superoxo species formed in enzymatic conditions exhibit several such H-bonding interactions, it is not surprising to see that the enzymes are more robust catalysts compared to model complexes.

Discussion

Oxygen activation is central to the function of metalloenzymes, and once oxygen binds to the metal, this forms the putative metal-superoxo species, which then goes on to convert to other species or trigger reactivity on its own. The formation and reactivity of metal-superoxo species are thus central to understanding the enzyme kinetics and have, therefore, very broad implications in breathing to oxidation catalysis.[6] Among others, the copper(II)-superoxo species has been found to play a pivotal role in many enzymes, such as PHM. Constructing several biomimetic models that aim to capture both the structure and function of these enzymes was attempted. Among others, TMPA-based (TMPA = tris (2-pyridyl methyl) amine) copper-superoxo complexes $\{^{(X1)(X2)}LCu(II)\text{–}O_2^{\bullet-}\}$ are one of many thoroughly studied models with minor ligand modifications offering substantial improvements in reactivity.

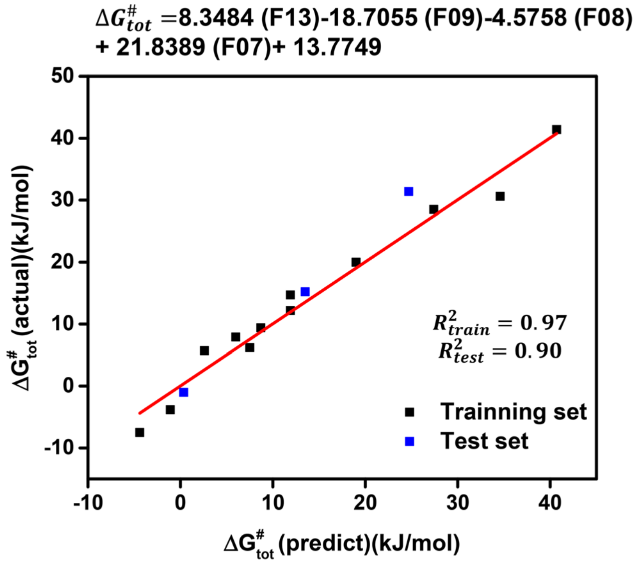

Fig. 7 The linear regression model performance for prediction of $\Delta G_{\mathrm{total}}$.

Furthermore, with five structurally analogous catalysts $\{^{(\mathrm{X1})(\mathrm{X2})}\mathrm{LCu(II)}{-}\mathrm{O_2}^{\bullet-}\}$ [X1 = H, X2 = H (**1a**), X1 = H, X2 = NH_2 (**2a**), X1 = NH_2, X2 = NH_2 (**3a**), X1 = NH(CO), X2 = H (**4a**) and X1 = X2 = NH(CO) (**5a**)] and three different substrates that were tested experimentally, this set of reactions offers a large treasure trove of data to benchmark the theory and develop potential machine learning models to untangle the relationship between enzymatic reactivity *vis-à-vis* biomimetic models, which has been the focus of this work. To elucidate the structure–activity relationship of the hydrogen atom transfer (HAT) reaction in metal-superoxo-mediated HAT catalysis, we initially constructed a sample space rooted in the experimental advances of analogous transformations. Subsequently, we conducted density functional theory (DFT) calculations on the devised sample space to generate the necessary statistical data for model training.

To begin with, we have computed the ground state geometries of catalysts **1a**–**5a** using DFT methods (B3LYP/TZVP), which yielded triplet (S = 1) ground states consistent with the experiments. The singlet state (S = 0) is higher in energy compared to the ground state by 100.5 kJ mol^{-1}, 96.2 kJ mol^{-1}, 100.8 kJ mol^{-1}, 93.5 kJ mol^{-1}, and 105.8 kJ mol^{-1} for **1a**–**5a**, respectively. To validate both the nature of the ground state and also obtain good numerical accuracy for the singlet–triplet gap that can be employed to judge the quality of the B3LYP results, we have undertaken *ab initio* DLPNO-CCSD(T) calculations on **1a**. This also consistently yields S = 1 as the ground state, with the singlet (S = 0) being 96.8 kJ mol^{-1} higher in energy, closely aligning with the results obtained from B3LYP. The spin densities determined for the atoms within catalyst **1a** using the DLPNO-CCSD(T) method closely agree with those obtained from B3LYP (as depicted in Fig. S29‡).

Furthermore, we have also investigated the dependence of the singlet–triplet gap ($\Delta G_{\mathrm{S-T}}$) on various exchange-correlation functionals, including GGA (BP86, PBE) and hybrid functionals (TPSSH, ω-B97X, PBE0) (refer to Tables S35 and S36‡). The GGA functional failed to accurately predict the gap (compared to DLPNO-CCSD(T) results), while the hybrid functionals exhibited similar trends across **1a**–**5a**, with changes of approximately 15 kJ mol^{-1} compared to the B3LYP functional. Additionally, single-point calculations conducted using B3LYP geometries and these functionals result in significantly smaller singlet–triplet gaps for the GGA functionals, while hybrid functionals produce consistent values. This strongly indicates that the energies are relatively less influenced by the geometries utilized and more by the nature of the exchange-correlation function employed. These findings align with earlier benchmark studies on copper-superoxide complexes.[93] Furthermore, Odoh and co-workers spearheaded a comprehensive method assessment, examining 31 functionals to determine their effectiveness in oxidizing methane with a tri-copper complex. Their findings underscored the importance of incorporating 20–30% Hartree–Fock exchange for achieving high accuracy.[93] Ugalde *et al.* delved into methane oxidation by copper hydroxide cations, revealing that single-reference functionals, incorporating a moderate amount of HF exchange, could yield methane activation barriers akin to those derived from multi-reference CASPT2.[94] Furthermore, many structural parameters observed are reproduced with the computation, offering confidence in the methodology (see Table S34‡). In particular, the ferromagnetic exchange between Cu(II) and the $\mathrm{O_2}^{\bullet-}$ species is relatively strong and is in the range of 1100 cm^{-1} to 1700 cm^{-1}. Due to trigonal bipyramidal geometry, the unpaired electron in the Cu(II) centre is found to be in the d_{z^2} orbital, which overlaps weakly with the π^* orbitals of the superoxo moiety, leading to degeneracy between π^*_σ and π^*_v orbitals and ferromagnetic coupling. Furthermore, the strength of the H-bonding interactions was found to vary significantly, and various analyses such as LOL, NCI, NBO, and AIM yield the following trend: **5a** > **4a** > **3a** > **2a** > **1a**. Coincidentally, the observed experimental reactivity also follows the same trend.

In the next step, we considered the reactivity by modelling the O–H activation of various substrates by the catalysts **1a**–**5a**, giving rise to fifteen combinations (**R1**–**R15**). In these reactions, the potential energy surface was modelled along with the stability of the $\{^{(\mathrm{X1})(\mathrm{X2})}\mathrm{LCu(II)}{-}\mathrm{O_2}^{\bullet-}\}$ species tested *via* competitive dimerization reactions. In particular, the O–H bond activation was found to proceed *via* a triplet transition state in all cases *via* the σ-HAT mechanism. During the transition state, one electron from the substrate was found to be transferred to the π^*_v orbital of the $\mathrm{O_2}^{\bullet-}$ radical leading to the elongation of the O–O bond, leading to the formation of respective phenoxy radicals in all cases. Our calculations predict the following reactivity order **5a** > **4a** > **1a** > **2a** > **3a** (termed ΔG_2) for all substrates. We assessed ΔG_2 using various other functionals, and found that all hybrid functionals exhibited similar patterns to B3LYP across **1a**–**5a** (see Table S37‡). However, this contradicts the experimental observations, which suggest catalyst **5a** to be the most reactive. As HAT reactions are subject to quantum tunnelling effects, we estimated the transmission coefficients for all the reactions, and these were found to be significant.

Our analysis reveals that tunnelling effects are correlated to the magnitude of the imaginary frequency (IF) computed. To understand the reason for the variation in the IF values, the asymmetry in the bond make–break O–H bond distance was estimated, and this is found to have a strong linear correlation, *i.e.* the greater the asymmetry, the wider the barrier, which in turn reduces the magnitude of the IF (see Fig. 8). A careful examination revealed that steric hindrance between the catalyst's substituents (amino/pivalamido) and substrate contributes to increased asymmetry, consequently lowering transmission coefficients. However, the incorporation of these effects still does not readily explain the trend observed.

We then extended our study not only to consider the O–H bond activation barriers but also a well-documented[11] competitive dimerization reaction and the corresponding transition state barrier (ΔG_3), which reduces the O–H bond activation rate. If these two parameters were taken into consideration together ($\Delta G_{\text{tot}} = \Delta G_2 - \Delta G_3$), we arrived at a predictive reactivity order of **1a** < **2a** < **3a** ~ **4a** < **5a**, which is in agreement with the experimental rate constant.[15] This suggests that not only the HAT step but also competitive catalyst poisoning needs to be carefully analyzed to understand their potent activity.

Estimating the ΔG_{tot} not only requires exploration of various mechanisms but also computationally challenging transition state geometries. Creating a model relying on basic descriptors to predict the reactivity of Cu(II)-superoxo species and directly determine the activation free energy (ΔG_{tot}) is crucial for enhancing understanding. For this purpose, we initially looked at the valence bond model that considers BDE energy as the descriptor, but, in our tested case, this is not comprehensive enough to rationalize the trend observed. We then moved to a machine-learning model comprising fifteen physical organic descriptors, as shown in Fig. 8. The descriptors are comprehensive and cover various aspects such as H-bonding, steric effects, thermodynamic properties, spin-state-dependent quantities, and acido-basic quantities. While many of the descriptors correlated well with the HAT trend observed, many failed to capture the complex mechanistic scenario hidden behind the ΔG_{tot} parameter. An iterative multivariate regression modelling process identified four quantum descriptors that predict the target variable T01 with an R^2 value of 0.90, RMSE of 4.01, and an MAE of 3.2 kJ mol^{-1} for the test set. Notably, the model developed hints at the importance of the pivotal role of H-bonding interactions in controlling the overall kinetics. Thermodynamic quantities such as ΔG_{PCET} and ΔG_{ET} exert more significant influence than the H-bonding interaction (HB) and ΔG_{PT} parameters. Specifically, HB interactions were found to have a greater impact than the ΔG_{PT} parameter, underscoring the significance of weak non-covalent interactions in modulating reactivity. The correlation analysis reveals that H-bonding strength is moderately correlated to the HAT step but rather strongly to the catalytic poisoning step by enhancing the corresponding kinetics requirements. The HAT reaction, on the other hand, relates very strongly with the ΔG_{PT} corresponding to the formation of Cu(III)-hydroperoxo species. Considering the fact that metal-superoxo species in metalloenzymes have a large number of H-bonding pockets coupled with an ability to seamlessly perform proton transfers, they could yield very small ΔG_{tot} and hence very high reactivity. Therefore, these considerations need to be incorporated into the ligand design if we aim to structurally and functionally mimic the metalloenzyme's reactivity. This study illustrates that combining DFT calculations with machine learning tools not only provides

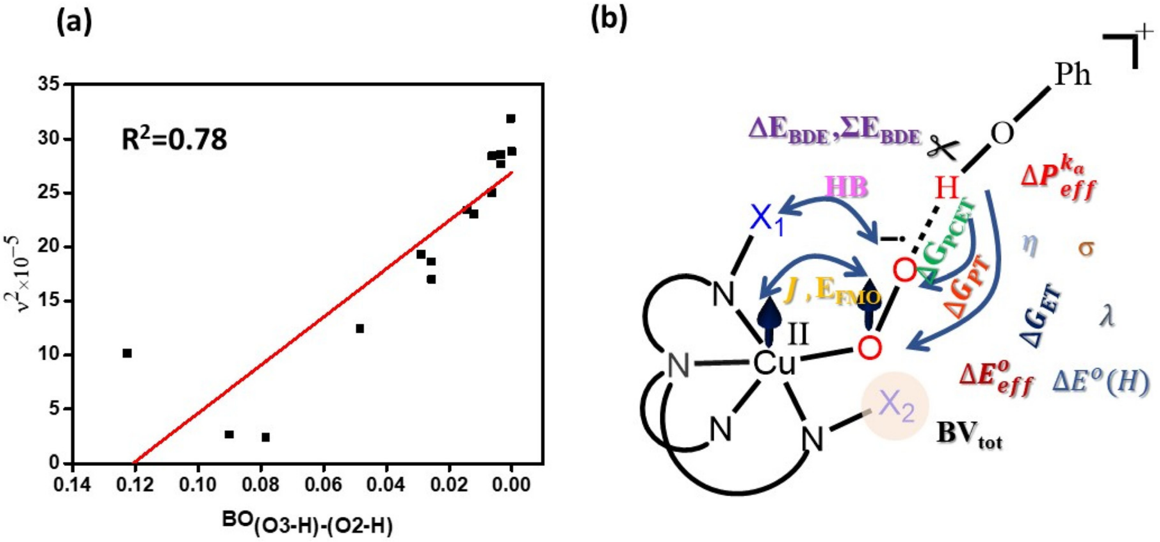

Fig. 8 (a) Correlation of the square of the imaginary frequency with the bond order (ν is the imaginary frequency and BO is the Wiberg bond order). (b) Schematic representation of encoding the catalyst structure and various quantum chemical descriptors employed here.

insight into the molecular mechanism but also reveals the anatomy of various factors governing overall reaction kinetics, which is an unprecedented approach in biomimetic chemistry.

Conclusions

Understanding the formation and reactivity of metal-superoxo species is crucial for enzyme kinetics, spanning processes from respiration to catalysis. The Cu(II)-superoxo complexes, particularly TMPA-based ones, serve as valuable biomimetic models, with minor ligand modifications enhancing their reactivity. Experimental data from five analogous catalysts ($\{^{(X1)(X2)}LCu(II)–O_2^{\bullet -}\}$ [X1 = H, X2 = H (**1a**), X1 = H, X2 = NH_2 (**2a**), X1 = NH_2, X2 = NH_2 (**3a**), X1 = NH(CO), X2 = H (**4a**) and X1 = X2 = NH(CO) (**5a**)] and different substrates provide a rich dataset for theory benchmarking and machine learning model development, elucidating the structure–activity relationship in metal-superoxo-mediated catalysis. Ground state geometries of catalysts **1a–5a**, determined through DFT calculations, exhibit triplet ground states consistent with experiments, with ferromagnetic exchange between Cu(II) and $O_2^{\bullet -}$ species and the strength of H-bonding interactions showing a trend of **5a** > **4a** > **3a** > **2a** > **1a**, mirroring experimentally observed reactivity towards the HAT reaction. Modelling O–H activation of various substrates by catalysts **1a–5a** revealed that HAT proceeds through the triplet transition states *via* the σ-HAT mechanism, yielding phenoxy radicals with a predicted reactivity order of **5a** > **4a** > **1a** > **2a** > **3a**, contrasting experimental observations. Quantum tunnelling effects, which are significant in HAT reactions, correlate with the magnitude of the imaginary frequency (IF) and asymmetry in the O–H bond distance of the transition state, with steric hindrance contributing to decreased transmission coefficients. Considering both O–H activation barriers and competitive dimerization reaction, a predictive reactivity order of **5a** > **4a** > **3a** > **2a** > **1a** emerged, aligning with experimental rate constants, emphasizing the importance of analyzing both HAT and catalyst poisoning for understanding reactivity. The development of a predictive model for Cu(II)-superoxo species reactivity (ΔG_{tot}) utilizing fifteen quantum chemical descriptors encompassing H-bonding, steric effects, and thermodynamic properties yielded an R^2 value of 0.90. This approach underscored the significance of H-bonding interactions in controlling kinetics, particularly in catalytic poisoning, rather than the HAT step, as revealed through correlation analysis. This study demonstrates that integrating DFT calculations with machine learning enables a comprehensive understanding of the molecular mechanism and the intricate interplay of factors governing overall reaction kinetics, offering unprecedented insights for biomimetic ligand design aimed at mimicking metalloenzyme reactivity. As enzymes such as galactose oxidase form cupric-superoxo species that contain several H-bonding interactions, our study suggests that the descriptor adapted here based on biomimetic models can also be utilized to understand enzyme kinetics and thus has scope beyond the examples presented.

Conflicts of interest

The authors declare no competing financial interest.

Acknowledgements

CSN thanks IIT Bombay for its fellowship and use of the HPC facility. GR would like to thank DST and SERB (SB/SJF/2019-20/12; CRG/2022/001697) for funding.

References

1 B. Kim, M. T. Brueggemeyer, W. J. Transue, Y. Park, J. Cho, M. A. Siegler, E. I. Solomon and K. D. Karlin, Fenton-like chemistry by a copper(I) complex and H_2O_2 relevant to enzyme peroxygenase C–H hydroxylation, *J. Am. Chem. Soc.*, 2023, **145**, 11735–11744.

2 D. Jeong, J. S. Valentine and J. Cho, Bio-inspired mononuclear nonheme metal peroxo complexes: Synthesis, structures and mechanistic studies toward understanding enzymatic reactions, *Coord. Chem. Rev.*, 2023, **480**, 215021.

3 P. Jiang, L. Zhang, X. Liu, C. Ye, P. Zhu, T. Tan, D. Wang and Y. Wang, Tuning oxidant and antioxidant activities of ceria by anchoring copper single-site for antibacterial application, *Nat. Commun.*, 2024, **15**, 1010.

4 J. Meng, H. Qin, H. Lei, X. Li, J. Fan, W. Zhang, U. P. Apfel and R. Cao, Adapting Synthetic Models of Heme/Cu Sites to Energy–Efficient Electrocatalytic Oxygen Reduction Reaction, *Angew. Chem., Int. Ed.*, 2023, **62**, e202312255.

5 B. Kim and K. D. Karlin, Ligand–Copper(I) Primary O2-Adducts: Design, Characterization, and Biological Significance of Cupric–Superoxides, *Acc. Chem. Res.*, 2023, **56**, 2197–2212.

6 E. A. Lewis and W. B. Tolman, Reactivity of dioxygen–copper systems, *Chem. Rev.*, 2004, **104**, 1047–1076.

7 B. F. Gherman, D. E. Heppner, W. B. Tolman and C. J. Cramer, Models for dioxygen activation by the CuB site of dopamine β-monooxygenase and peptidylglycine α-hydroxylating monooxygenase, *J. Biol. Inorg. Chem.*, 2006, **11**, 197–205.

8 S. Itoh, Mononuclear copper active-oxygen complexes, *Curr. Opin. Chem. Biol.*, 2006, **10**, 115–122.

9 P. Chen and E. I. Solomon, O2 activation by binuclear Cu sites: noncoupled versus exchange coupled reaction mechanisms, *Proc. Natl. Acad. Sci. U. S. A.*, 2004, **101**, 13105–13110.

10 L. M. Mirica, X. Ottenwaelder and T. D. P. Stack, Structure and spectroscopy of copper– dioxygen complexes, *Chem. Rev.*, 2004, **104**, 1013–1046.

11 C. E. Elwell, N. L. Gagnon, B. D. Neisen, D. Dhar, A. D. Spaeth, G. M. Yee and W. B. Tolman, Copper–oxygen complexes revisited: structures, spectroscopy, and reactivity, *Chem. Rev.*, 2017, **117**, 2059–2107.

12 J. G. Kleingardner and K. L. Bren, Biological significance and applications of heme c proteins and peptides, *Acc. Chem. Res.*, 2015, **48**, 1845–1852.

13 J. P. Klinman, Mechanisms whereby mononuclear copper proteins functionalize organic substrates, *Chem. Rev.*, 1996, **96**, 2541–2562.

14 P. Chen and E. I. Solomon, Oxygen activation by the noncoupled binuclear copper site in peptidylglycine α-hydroxylating monooxygenase. Reaction mechanism and role of the noncoupled nature of the active site, *J. Am. Chem. Soc.*, 2004, **126**, 4991–5000.

15 D. E. Diaz, D. A. Quist, A. E. Herzog, A. W. Schaefer, I. Kipouros, M. Bhadra, E. I. Solomon and K. D. Karlin, Impact of Intramolecular Hydrogen Bonding on the Reactivity of Cupric Superoxide Complexes with O– H and C– H Substrates, *Angew. Chem.*, 2019, **131**, 17736–17740.

16 J. P. Evans, K. Ahn and J. P. Klinman, Evidence that dioxygen and substrate activation are tightly coupled in dopamine β-monooxygenase: implications for the reactive oxygen species, *J. Biol. Chem.*, 2003, **278**, 49691–49698.

17 P. Chen, J. Bell, B. A. Eipper and E. I. Solomon, Oxygen Activation by the Noncoupled Binuclear Copper Site in Peptidylglycine α-Hydroxylating Monooxygenase. Spectroscopic Definition of the Resting Sites and the Putative CuIIM– OOH Intermediate, *Biochemistry*, 2004, **43**, 5735–5747.

18 Y. Liu, A. Mukherjee, N. Nahumi, M. Ozbil, D. Brown, A. M. Angeles-Boza, D. M. Dooley, R. Prabhakar and J. P. Roth, Experimental and computational evidence of metal-O2 activation and rate-limiting proton-coupled electron transfer in a copper amine oxidase, *J. Phys. Chem. B*, 2013, **117**, 218–229.

19 S. Itoh and K. D. Karlin, *Copper-oxygen chemistry*, Wiley, 2011.

20 K. J. Humphreys, L. M. Mirica, Y. Wang and J. P. Klinman, Galactose oxidase as a model for reactivity at a copper superoxide center, *J. Am. Chem. Soc.*, 2009, **131**, 4657–4663.

21 R. E. Cowley, L. Tian and E. I. Solomon, Mechanism of O2 activation and substrate hydroxylation in noncoupled binuclear copper monooxygenases, *Proc. Natl. Acad. Sci. U. S. A.*, 2016, **113**, 12035–12040.

22 S. Itoh, Developing mononuclear copper–active-oxygen complexes relevant to reactive intermediates of biological oxidation reactions, *Acc. Chem. Res.*, 2015, **48**, 2066–2074.

23 M. Schatz, V. Raab, S. P. Foxon, G. Brehm, S. Schneider, M. Reiher, M. C. Holthausen, J. Sundermeyer and S. Schindler, Combined Spectroscopic and Theoretical Evidence for a Persistent End–On Copper Superoxo Complex, *Angew. Chem., Int. Ed.*, 2004, **43**, 4360–4363.

24 T. Punniyamurthy, S. Velusamy and J. Iqbal, Recent advances in transition metal catalyzed oxidation of organic substrates with molecular oxygen, *Chem. Rev.*, 2005, **105**, 2329–2364.

25 B. F. Gherman and C. J. Cramer, Modeling the peroxide/superoxide continuum in 1: 1 side-on adducts of O2 with Cu, *Inorg. Chem.*, 2004, **43**, 7281–7283.

26 M. Mandal, C. E. Elwell, C. J. Bouchey, T. J. Zerk, W. B. Tolman and C. J. Cramer, Mechanisms for hydrogen-atom abstraction by mononuclear copper(III) cores: Hydrogen-atom transfer or concerted proton-coupled electron transfer?, *J. Am. Chem. Soc.*, 2019, **141**, 17236–17244.

27 A. C. Aragones, N. L. Haworth, N. Darwish, S. Ciampi, N. J. Bloomfield, G. G. Wallace, I. Diez-Perez and M. L. Coote, Electrostatic catalysis of a Diels–Alder reaction, *Nature*, 2016, **531**, 88–91.

28 P. Comba, C. Haaf, S. Helmle, K. D. Karlin, S. Pandian and A. Waleska, Dioxygen reactivity of new bispidine-copper complexes, *Inorg. Chem.*, 2012, **51**, 2841–2851.

29 J. J. Liu, D. E. Diaz, D. A. Quist and K. D. Karlin, Copper(I)–Dioxygen Adducts and Copper Enzyme Mechanisms, *Isr. J. Chem.*, 2016, **56**, 738–755.

30 J. Y. Lee and K. D. Karlin, Elaboration of copper–oxygen mediated C–H activation chemistry in consideration of future fuel and feedstock generation, *Curr. Opin. Chem. Biol.*, 2015, **25**, 184–193.

31 M. Weitzer, S. Schindler, G. Brehm, S. Schneider, E. Hörmann, B. Jung, S. Kaderli and A. D. Zuberbühler, Reversible binding of dioxygen by the copper(I) complex with tris (2-dimethylaminoethyl) amine (Me6tren) ligand, *Inorg. Chem.*, 2003, **42**, 1800–1806.

32 H. C. Fry, D. V. Scaltrito, K. D. Karlin and G. J. Meyer, The rate of O2 and CO binding to a copper complex, determined by a "flash-and-trap" technique, exceeds that for hemes, *J. Am. Chem. Soc.*, 2003, **125**, 11866–11871.

33 D.-H. Lee, N. N. Murthy and K. D. Karlin, Binuclear Copper Complexes Based on the 6,6′-Bis [[bis (2-pyridylmethyl) amino] methyl]-2,2′-bipyridine Ligand, *Inorg. Chem.*, 1997, **36**, 5785–5792.

34 D. Maiti, J. S. Woertink, A. A. Narducci Sarjeant, E. I. Solomon and K. D. Karlin, Copper dioxygen adducts: formation of bis (μ-oxo) dicopper(III) versus (μ-1, 2) peroxodicopper(II) complexes with small changes in one pyridylligand substituent, *Inorg. Chem.*, 2008, **47**, 3787–3800.

35 K. D. Karlin, N. Wei, B. Jung, S. Kaderli, P. Niklaus and A. D. Zuberbuehler, Kinetics and thermodynamics of formation of copper-dioxygen adducts: Oxygenation of mononuclear copper(I) complexes containing tripodal tetradentate ligands, *J. Am. Chem. Soc.*, 1993, **115**, 9506–9514.

36 R. L. Peterson, R. A. Himes, H. Kotani, T. Suenobu, L. Tian, M. A. Siegler, E. I. Solomon, S. Fukuzumi and K. D. Karlin, Cupric superoxo-mediated intermolecular C– H activation chemistry, *J. Am. Chem. Soc.*, 2011, **133**, 1702–1705.

37 M. Bhadra, J. Y. C. Lee, R. E. Cowley, S. Kim, M. A. Siegler, E. I. Solomon and K. D. Karlin, Intramolecular hydrogen bonding enhances stability and reactivity of mononuclear cupric superoxide complexes, *J. Am. Chem. Soc.*, 2018, **140**, 9042–9045.

38 M. A. Ehudin, A. W. Schaefer, S. M. Adam, D. A. Quist, D. E. Diaz, J. A. Tang, E. I. Solomon and K. D. Karlin, Influence of intramolecular secondary sphere hydrogen-bonding interactions on cytochrome c oxidase inspired

low-spin heme–peroxo–copper complexes, *Chem. Sci.*, 2019, **10**, 2893–2905.

39 K. T. Butler, D. W. Davies, H. Cartwright, O. Isayev and A. Walsh, Machine learning for molecular and materials science, *Nature*, 2018, **559**, 547–555.

40 L.-C. Yang, X. Li, S.-Q. Zhang and X. Hong, Machine learning prediction of hydrogen atom transfer reactivity in photoredox-mediated C–H functionalization, *Org. Chem. Front.*, 2021, **8**, 6187–6195.

41 J. E. Schneider, M. K. Goetz and J. S. Anderson, Statistical analysis of C–H activation by oxo complexes supports diverse thermodynamic control over reactivity, *Chem. Sci.*, 2021, **12**, 4173–4183.

42 W. Lai, C. Li, H. Chen and S. Shaik, Hydrogen–abstraction reactivity patterns from A to Y: The valence bond way, *Angew. Chem., Int. Ed.*, 2012, **51**, 5556–5578.

43 J. England, Y. Guo, K. M. Van Heuvelen, M. A. Cranswick, G. T. Rohde, E. L. Bominaar, E. Münck and L. Que Jr., A more reactive trigonal-bipyramidal high-spin oxoiron(IV) complex with a cis-labile site, *J. Am. Chem. Soc.*, 2011, **133**, 11880–11883.

44 J. England, M. Martinho, E. R. Farquhar, J. R. Frisch, E. L. Bominaar, E. Münck and L. Que Jr., A synthetic high–spin oxoiron(IV) complex: generation, spectroscopic characterization, and reactivity, *Angew. Chem.*, 2009, **121**, 3676–3680.

45 J. P. Bigi, W. H. Harman, B. Lassalle-Kaiser, D. M. Robles, T. A. Stich, J. Yano, R. D. Britt and C. J. Chang, A high-spin iron(IV)–oxo complex supported by a trigonal nonheme pyrrolide platform, *J. Am. Chem. Soc.*, 2012, **134**, 1536–1542.

46 D. Bím, M. Maldonado-Domínguez, L. Rulíšek and M. Srnec, Beyond the classical thermodynamic contributions to hydrogen atom abstraction reactivity, *Proc. Natl. Acad. Sci. U. S. A.*, 2018, **115**, E10287–E10294.

47 D. Bím, M. Maldonado-Domínguez, R. Fučík and M. Srnec, Dissecting the Temperature Dependence of Electron–Proton Transfer Reactivity, *J. Phys. Chem. C*, 2019, **123**, 21422–21428.

48 M. Maldonado-Domínguez, D. Bím, R. Fučík, R. Čurík and M. Srnec, Reactive mode composition factor analysis of transition states: The case of coupled electron–proton transfers, *Phys. Chem. Chem. Phys.*, 2019, **21**, 24912–24918.

49 W. D. Bailey, D. Dhar, A. C. Cramblitt and W. B. Tolman, Mechanistic dichotomy in proton-coupled electron-transfer reactions of phenols with a copper superoxide complex, *J. Am. Chem. Soc.*, 2019, **141**, 5470–5480.

50 H. Chen, W. Lai and S. Shaik, Exchange-Enhanced H-Abstraction Reactivity of High-Valent Nonheme Iron(IV)-Oxo from Coupled Cluster and Density Functional Theories, *J. Phys. Chem. Lett.*, 2010, **1**, 1533–1540.

51 D. G. Liakos and F. Neese, Interplay of Correlation and Relativistic Effects in Correlated Calculations on Transition-Metal Complexes: The (Cu2O2)2+ Core Revisited, *J. Chem. Theory Comput.*, 2011, **7**, 1511–1523.

52 M. He, J. Zhang, X.-L. Sun, B.-H. Chen and Y.-G. Wang, Theoretical Study on Methane Oxidation Catalyzed by Fe/ZSM-5: The Significant Role of Water on Binuclear Iron Active Sites, *J. Phys. Chem. C*, 2016, **120**, 27422–27429.

53 M. J. Frisch, G. W. Trucks, H. B. Schlegel, G. E. Scuseria, M. A. Robb, J. R. Cheeseman, G. Scalmani, V. Barone, B. Mennucci and G. Petersson, *Gaussian 09, Revision D. 01*, Gaussian, Inc., Wallingford CT, 2009, see also: URL: **https://www.gaussian.com**.

54 T. Lu and F. Chen, Multiwfn: a multifunctional wavefunction analyzer, *J. Comput. Chem.*, 2012, **33**, 580–592.

55 W. Humphrey, A. Dalke and K. Schulten, VMD: visual molecular dynamics, *J. Mol. Graphics*, 1996, **14**, 33–38.

56 J. Bigeleisen, The relative reaction velocities of isotopic molecules, *J. Chem. Phys.*, 1949, **17**, 675–678.

57 D. Ferro-Costas, D. G. Truhlar and A. Fernández-Ramos, Pilgrim: A thermal rate constant calculator and a chemical kinetics simulator, *Comput. Phys. Commun.*, 2020, **256**, 107457.

58 M. Page and J. W. McIver Jr., On evaluating the reaction path Hamiltonian, *J. Chem. Phys.*, 1988, **88**, 922–935.

59 Y. Freund and R. E. Schapire, A decision-theoretic generalization of on-line learning and an application to boosting, *J. Comput. Syst. Sci.*, 1997, **55**, 119–139.

60 L. Breiman, Random forests, *Mach. Learn.*, 2001, **45**, 5–32.

61 S. Zhong, K. Zhang, D. Wang and H. Zhang, Shedding light on "Black Box" machine learning models for predicting the reactivity of HO radicals toward organic compounds, *Chem. Eng. J.*, 2021, **405**, 126627.

62 W. Xu, F. Long, H. Zhao, Y. Zhang, D. Liang, L. Wang, K. L. Lesnik, H. Cao, Y. Zhang and H. Liu, Performance prediction of ZVI-based anaerobic digestion reactor using machine learning algorithms, *Waste Manag.*, 2021, **121**, 59–66.

63 F. Neese, Software update: the ORCA program system, version 4.0, *Wiley Interdiscip. Rev.: Comput. Mol. Sci.*, 2018, **8**, e1327.

64 S. E. Neale, D. A. Pantazis and S. A. Macgregor, Accurate computed spin-state energetics for Co(iii) complexes: implications for modelling homogeneous catalysis, *Dalton Trans.*, 2020, **49**, 6478–6487.

65 F. Neese, F. Wennmohs, U. Becker and C. Riplinger, The ORCA quantum chemistry program package, *J. Chem. Phys.*, 2020, **152**, 224108.

66 A. D. Becke, Density-functional thermochemistry. V. Systematic optimization of exchange-correlation functionals, *J. Chem. Phys.*, 1997, **107**, 8554–8560.

67 J. Antony and S. Grimme, Density functional theory including dispersion corrections for intermolecular interactions in a large benchmark set of biologically relevant molecules, *Phys. Chem. Chem. Phys.*, 2006, **8**, 5287–5293.

68 A. D. Becke, Density-functional exchange-energy approximation with correct asymptotic behavior, *Phys. Rev. A*, 1988, **38**, 3098–3100.

69 P. A. Frey, Strong hydrogen bonding in molecules and enzymatic complexes, *J. Magn. Reson.*, 2001, **39**, S190–S198.

70 S. Emamian, T. Lu, H. Kruse and H. Emamian, Exploring nature and predicting strength of hydrogen bonds: A corre-

lation analysis between atoms–in–molecules descriptors, binding energies, and energy components of symmetry–adapted perturbation theory, *J. Comput. Chem.*, 2019, **40**, 2868–2881.

71 R. Bader, *A quantum theory*, Clarendon, Oxford, UK, 1990.

72 H. L. Schmider and A. D. Becke, Chemical content of the kinetic energy density, *J. Mol. Struct.: THEOCHEM*, 2000, **527**, 51–61.

73 G. Saleh, C. Gatti, L. Lo Presti and J. Contreras-García, Revealing non–covalent interactions in molecular crystals through their experimental electron densities, *Chem. – Eur. J.*, 2012, **18**, 15523–15536.

74 D. Mandal, R. Ramanan, D. Usharani, D. Janardanan, B. Wang and S. Shaik, How does tunneling contribute to counterintuitive H-abstraction reactivity of nonheme Fe(IV) O oxidants with alkanes?, *J. Am. Chem. Soc.*, 2015, **137**, 722–733.

75 D. Mandal and S. Shaik, Interplay of Tunneling, Two-State Reactivity, and Bell–Evans–Polanyi Effects in C–H Activation by Nonheme Fe(IV) O Oxidants, *J. Am. Chem. Soc.*, 2016, **138**, 2094–2097.

76 J. E. Klein, D. Mandal, W.-M. Ching, D. Mallick, L. Que Jr. and S. Shaik, Privileged role of thiolate as the axial ligand in hydrogen atom transfer reactions by oxoiron(IV) complexes in shaping the potential energy surface and inducing significant H-atom tunneling, *J. Am. Chem. Soc.*, 2017, **139**, 18705–18713.

77 Y. H. Kwon, B. K. Mai, Y.-M. Lee, S. N. Dhuri, D. Mandal, K.-B. Cho, Y. Kim, S. Shaik and W. Nam, Determination of spin inversion probability, H-tunneling correction, and regioselectivity in the two-state reactivity of nonheme iron (IV)-oxo complexes, *J. Phys. Chem. Lett.*, 2015, **6**, 1472–1476.

78 E. J. Klinker, S. Shaik, H. Hirao and L. Que Jr., A Two–State Reactivity Model Explains Unusual Kinetic Isotope Effect Patterns in C═H Bond Cleavage by Nonheme Oxoiron(IV) Complexes, *Angew. Chem., Int. Ed.*, 2009, **48**, 1291–1295.

79 D. Mandal, D. Mallick and S. Shaik, Kinetic isotope effect determination probes the spin of the transition state, its stereochemistry, and its ligand sphere in hydrogen abstraction reactions of oxoiron(IV) complexes, *Acc. Chem. Res.*, 2018, **51**, 107–117.

80 S. Yamaguchi, A. Wada, Y. Funahashi, S. Nagatomo, T. Kitagawa, K. Jitsukawa and H. Masuda, Thermal Stability and Absorption Spectroscopic Behavior of (μ–Peroxo) dicopper Complexes Regulated with Intramolecular Hydrogen Bonding Interactions, *Eur. J. Inorg. Chem.*, 2003, **2003**, 4378–4386.

81 R. R. Jacobson, Z. Tyeklar, A. Farooq, K. D. Karlin, S. Liu and J. Zubieta, A copper-oxygen (Cu2-O2) complex. Crystal structure and characterization of a reversible dioxygen binding system, *J. Am. Chem. Soc.*, 1988, **110**, 3690–3692.

82 S. Zhong, K. Zhang, M. Bagheri, J. G. Burken, A. Gu, B. Li, X. Ma, B. L. Marrone, Z. J. Ren and J. Schrier, Machine learning: new ideas and tools in environmental science and engineering, *Environ. Sci. Technol.*, 2021, **55**, 12741–12754.

83 D. Cha, S. Park, M. S. Kim, T. Kim, S. W. Hong, K. H. Cho and C. Lee, Prediction of oxidant exposures and micropollutant abatement during ozonation using a machine learning method, *Environ. Sci. Technol.*, 2020, **55**, 709–718.

84 G. Yu, Y. Wu, H. Cao, Q. Ge, Q. Dai, S. Sun and Y. Xie, Insights into the mechanism of ozone activation and singlet oxygen generation on N-doped defective nanocarbons: A DFT and machine learning study, *Environ. Sci. Technol.*, 2022, **56**, 7853–7863.

85 P. Su, L. Song, W. Wu, P. C. Hiberty and S. Shaik, Valence bond calculations of hydrogen transfer reactions: a general predictive pattern derived from theory, *J. Am. Chem. Soc.*, 2004, **126**, 13539–13549.

86 A. Sen, A. Ansari, A. Swain, B. Pandey and G. Rajaraman, Probing the Origins of Puzzling Reactivity in Fe/Mn–Oxo/Hydroxo Species toward C–H Bonds: A DFT and Ab Initio Perspective, *Inorg. Chem.*, 2023, **62**, 14931–14941.

87 V. Krewald, M. Retegan, N. Cox, J. Messinger, W. Lubitz, S. DeBeer, F. Neese and D. A. Pantazis, Metal oxidation states in biological water splitting, *Chem. Sci.*, 2015, **6**, 1676–1695.

88 L. Noodleman and W.-G. Han, Structure, redox, pKa, spin. A golden tetrad for understanding metalloenzyme energetics and reaction pathways, *J. Biol. Inorg. Chem.*, 2006, **11**, 674–694.

89 A. Ansari, P. Jayapal and G. Rajaraman, C═H Bond Activation by Metal–Superoxo Species: What Drives High Reactivity?, *Angew. Chem.*, 2015, **127**, 574–578.

90 M. Bhadra, J. Y. C. Lee, R. E. Cowley, S. Kim, M. A. Siegler, E. I. Solomon and K. D. Karlin, Intramolecular Hydrogen Bonding Enhances Stability and Reactivity of Mononuclear Cupric Superoxide Complexes, *J. Am. Chem. Soc.*, 2018, **140**, 9042–9045.

91 M. Salamone, M. Galeotti, E. Romero-Montalvo, J. A. van Santen, B. D. Groff, J. M. Mayer, G. A. DiLabio and M. Bietti, Bimodal Evans–Polanyi relationships in hydrogen atom transfer from C (sp3)–H bonds to the cumyloxyl radical. A combined time-resolved kinetic and computational study, *J. Am. Chem. Soc.*, 2021, **143**, 11759–11776.

92 Y. Liu, X. Zong, A. Patra, S. Caratzoulas and D. G. Vlachos, Propane Dehydrogenation on PtxSny (x, y ≤ 4) Clusters on Al_2O_3(110), *ACS Catal.*, 2023, **13**, 2802–2812.

93 N. K. Dandu, J. A. Reed and S. O. Odoh, Performance of Density Functional Theory for Predicting Methane-to-Methanol Conversion by a Tri-Copper Complex, *J. Phys. Chem. C*, 2018, **122**, 1024–1036.

94 E. Rezabal, F. Ruipérez and J. M. Ugalde, Quantum chemical study of the catalytic activation of methane by copper oxide and copper hydroxide cations, *Phys. Chem. Chem. Phys.*, 2013, **15**, 1148–1153.